




EARTH SCIENCES

Lithosphere architecture characterized by crust–mantle decoupling controls the formation of orogenic gold deposits

Zengqian Hou^{1,*}, Qingfei Wang^{2,*}, Haijiang Zhang^{3,*}, Bo Xu², Nian Yu⁴, Rui Wang ², David I. Groves^{2,5}, Yuanchuan Zheng², Shoucheng Han ³, Lei Gao ³ and Lin Yang²

¹Institute of Geology, Chinese Academy of Geological Sciences, Beijing 100037, China;

²State Key Laboratory of Geological

Processes and

Mineral Resources,

China University of

Geosciences (Beijing),

Beijing 100083, China;

³School of Earth and Space Sciences,

University of Science

and Technology of

China, Hefei 230026,

China; ⁴School of

Electrical Engineering,

Chongqing University,

Chongqing 400044,

China and ⁵Centre for

Exploration Targeting,

University of Western

Australia, Crawley

6009, Australia

*Corresponding

authors. E-mails:

houzengqian@126.com;

wqf@cugb.edu.cn;

zhang11@ustc.edu.cn

Received 8 July

2022; Revised 31

October 2022;

Accepted 8

November 2022

ABSTRACT

This study, via combined analysis of geophysical and geochemical data, reveals a lithospheric architecture characterized by crust–mantle decoupling and vertical heat-flow conduits that control orogenic gold mineralization in the Ailaoshan gold belt on the southeastern margin of Tibet. The mantle seismic tomography indicates that the crust–mantle decoupled deformation, defined from previous seismic anisotropy analysis, was formed by upwelling and lateral flow of the asthenosphere, driven by deep subduction of the Indian continent. Our magnetotelluric and seismic images show both a vertical conductor across the Moho and high V_p/V_s anomalies both in the uppermost mantle and lowest crust, suggesting that crust–mantle decoupling promotes ponding of mantle-derived basic melts at the base of the crust via a heat-flow conduit. Noble gas isotope and halogen ratios of gold-related ore minerals indicate a mantle source of ore fluid. A rapid decrease in Cl/F ratios of lamprophyres under conditions of 1.2 GPa and 1050°C suggests that the ore fluid was derived from degassing of the basic melts. Similar lithospheric architecture is recognized in other orogenic gold provinces, implying analogous formational controls.

Keywords: crust–mantle decoupling, lithosphere architecture, orogenic gold deposit, seismic tomography, magnetotelluric imaging, Tibet

INTRODUCTION

Orogenic gold deposits (OGDs), which supply ~30% of our gold resources worldwide, were formed by massive aqueous-carbonic fluid flow along major fault zones during orogeny [1]. Such OGDs formed abundantly in Precambrian greenstone belts during periods of continental growth associated with episodic mantle plumes [2]. Their auriferous ore fluids are traditionally regarded to be derived from dehydration of crustal rocks during prograde metamorphism [1,3–5]. However, there is increasing evidence for the existence of Phanerozoic OGDs that are sited on the margins of Archean cratons (Fig. 1a) [4–9], which usually underwent destruction or reworking due to later oceanic subduction and/or continental collision [9–12] on these margins. These OGDs normally postdated

regional prograde metamorphism and were concomitant with mafic dyke swarms [4,13]. Typical examples include the Early Cretaceous OGDs, such as at Apsaka in the Siberian Craton [14] and the Jiaodong Peninsula in the North China Craton [15–17], as well as the Cenozoic OGDs in the Ailaoshan gold belt in the Yangtze Craton [18–21]. Their ore fluids, although contentious [22], were argued to have been derived from a sub-crustal source, with a strong mantle lithosphere affinity [17,23–25]. In view of this, comprehensive studies on the architecture of the lithosphere and geological processes within it are necessary to understand the genesis of such orogenic gold deposits [1,2,11].

The Cenozoic Ailaoshan gold belt, on the southeastern margin of Tibet (Fig. 1b), is an ideal terrane to test and constrain genetic models for such gold deposits. This is because the gold

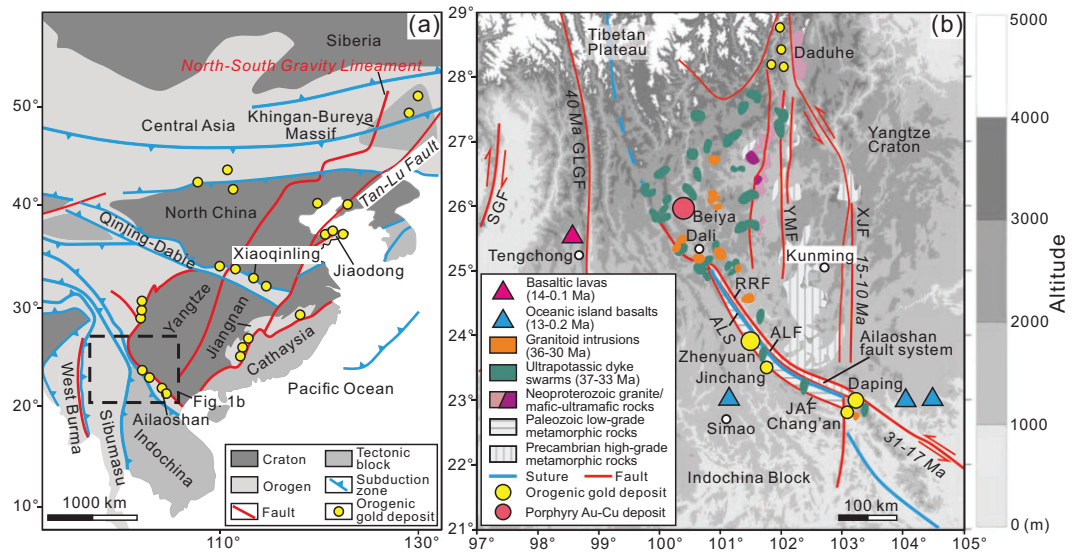


Figure 1. (a) Eastern Asia cratons showing Precambrian blocks (Stanovoy, Khingan-Bureya, North China, Yangtze, Cathaysia) and Phanerozoic orogenic gold provinces at their edges (modified from ref. [4]). (b) Tectonic framework of the eastern Indo-Asian collisional zone (modified from ref. [37]), bounded by Cenozoic faults with ages labeled (ALF: Ailaoshan fault; GLGF: Gaoligong fault; LMT: Longenshan thrust fault; SGF: Sagaing fault; RRF: Red-River fault; XJF: Xiaojiang fault; YMF: Yuan-Yuan-Muliou fault). Four large orogenic gold deposits (e.g. Zhenyuan, Jinchang, Chang'an and Daping) and the associated Cenozoic igneous rocks along the RRF are shown. A world-class porphyry gold deposit at Beiya and a gold prospect along the Dadu River are shown for comparison.

mineralization formed in this belt is anomalously young and well preserved, with the underlying lithosphere most likely to represent that at the time the gold deposits formed. Related previous research includes crustal deformation analysis [26,27], seismic and magnetotelluric (MT) imaging of the lithosphere [28–33], petrological investigation of Cenozoic igneous rocks [34,35], and systematic isotope analyses related to the genesis of OGDs [6]. These data suggest that decoupling of the crust and mantle occurred during deformation, and that low velocity and resistivity anomalies developed at different depths in this region. Although not definitive, the isotopic signatures of sulfur and oxygen for the OGDs imply mantle derivation of the auriferous ore fluid. However, the nature of mantle–crust architecture and its tectonic drivers, especially the nature of the control by lithosphere on the OGDs, was not previously well defined. In this study, we have improved this understanding by reconstructing and refining lithosphere structure utilizing more advanced seismic and MT imaging methods with more densely spaced stations, and by obtaining robust geochemical data, including noble gas (He, Ar, Kr, Xe) and halogen (Cl, F, Br, I) data for gold ores and spatially associated lamprophyres. Our results reveal a lithosphere structure characterized by crust–mantle decoupling with high-flux conduit systems across the Moho, which promoted ponding and degassing of hydrous

mantle melts at the mantle–crust transition and controlled the formation of the OGDs.

GEOLOGICAL BACKGROUND

Ailaoshan, the largest orogenic gold belt in SW China, is located on the southeastern margin of the Tibetan Plateau, which is built on a tectonic collage of continental blocks, including the Sibumasu, Indochina and Yangtze blocks, that amalgamated due to Triassic Paleo-Tethyan and Cenozoic Neo-Tethyan closures [36]. Its tectonic evolution was primarily controlled by the Cenozoic Indo-Asian collision, which resulted in numerous strike-slip faults with block extrusion and Eocene-Miocene magmatism (Fig. 1b).

The Ailaoshan gold belt is controlled by a series of Cenozoic strike-slip faults, including the Red-River fault (RRF), Ailaoshan fault (ALF) and Anding fault (ADF) (Fig. 1b) [37]. This gold belt was developed in juxtaposed high-grade (east) and low-grade (west) metamorphic zones bounded by the ALF. The protolith of the former were largely Neoproterozoic volcanic-sedimentary rocks, recording oceanic subduction beneath the Yangtze Craton [38], whereas the latter is composed of Paleozoic strata and Paleo-Tethyan ophiolitic melanges [39], representing tectonic relics of the Paleo-Tethyan Ocean. The eastern high-grade metamorphic zone

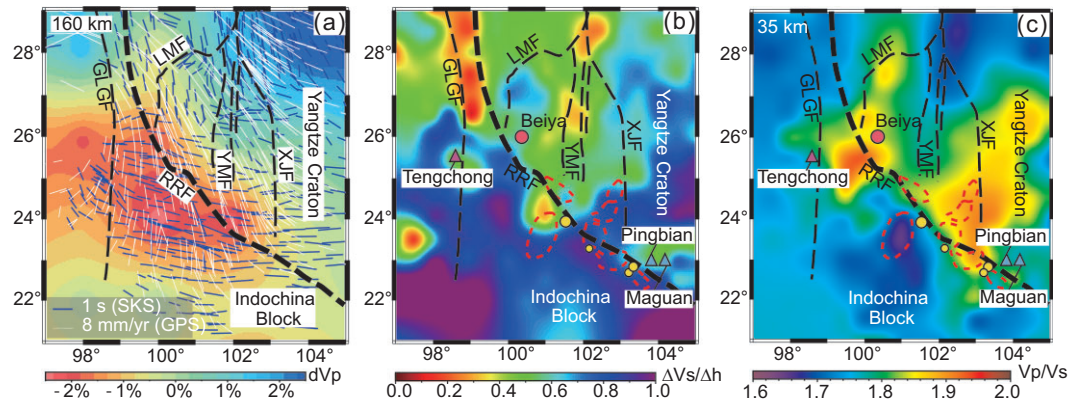


Figure 2. (a) A depth slice of P-velocity image at 160 km. Bounded at $\sim 26^\circ\text{N}$, a major low-velocity anomaly at 160 km depth occurs in the southern part with nearly E-W-trending fast directions in mantle (blue line) by SKS shear wave splitting measurements [28,30,72] and nearly N-S-trending surface displacement vectors (white line) by GPS measurements [26,27]. This image shows the lithosphere decoupling deformation induced by the upwelling asthenosphere. (b) Variation in $\Delta V_s/\Delta h$ near the Moho. The low-resistivity bodies near the Moho [33] are shown for comparison. For explanations see the text. (c) Variation in V_p/V_s ratios near the actual Moho, reflecting main sites for underplating of basic melts at the crust–mantle boundary interface along the Ailaoshan belt. Abbreviations for fault names are the same as those in Fig. 1.

experienced amphibolite-granulite facies metamorphism peaking at 44–36 Ma [40,41], followed by near-isothermal decompression at 32–25 Ma and retrograde metamorphism at 25–14 Ma [42]. Due to the India-Asia collision, extrusion of the Indochina block initiated left-lateral shearing along the RRF at 34–30 Ma [40,41,43]. The Eocene ultrapotassic lamprophyre dike swarms (37–28 Ma) with minor granite (used *sensu lato* throughout) stocks (36–30 Ma) intruded at about the same time along the RRF [44,45]. The gold mineralization that is spatially associated with Eocene ultrapotassic magmatism forms numerous large gold deposits, such as the Zhenyuan, Chang’an and Daping deposits (Fig. 1b) [18,20], which are sited in the folded pre-Triassic low-grade metamorphic zone that is bounded by the ADF and ALF (Fig. 1b).

The gold deposits in the Ailaoshan gold belt have features characteristic of OGDs, with two styles of mineralization [18]: quartz vein deposits such as Daping and disseminated ores such as Zhenyuan, Chang’an and Jinchang. Robust radiogenic isotope data define a range of mineralization ages of 45 to 26 Ma [37,46–48], except for the Jinchang deposit with a fuchsite $^{40}\text{Ar}/^{39}\text{Ar}$ age of ca. 60 Ma [49]. Similar timing of gold mineralization is also recorded from the northwestern margin of the Yangtze Craton, where the Dadu River gold prospect with mineralization ages of 30–20 Ma is controlled by the Cenozoic Xiaojiang fault (XJF) system [50]. In addition, the world-class Beiya porphyry gold deposit is spatially and probably genetically associated with Eocene granite stocks and lamprophyre dikes (36–32 Ma) near Dali (Fig. 1b) [51,52].

RESULTS

Seismic velocity structure and V_p/V_s model

A large magnitude low-velocity anomaly is imaged to the south of latitude 26°N at a depth of 160 km by mantle seismic tomography (Fig. 2a). Along the profile at latitude 24°N , this low-velocity anomaly is located on the eastern side of the subducted Indian continent and lies beneath the Asian lithosphere (Indochina and Yangtze) at longitude 97°E – 106°E , both of which are imaged as high-velocity anomalies (Fig. 3a). This low-velocity anomaly extends upwards to ~ 80 km depth and downwards into the mantle transition zone (Fig. 3a).

The V_p and V_s models from joint inversion of body wave arrival times, surface wave dispersion curves, and receiver functions clearly show a middle-crustal (av 20 km in depth) P-wave and S-wave low-velocity layer (Fig. S1) corresponding to high V_p/V_s values (Fig. S2) and low-resistivity anomalies (Fig. 3c) beneath the Ailaoshan gold belt. The low-velocity layer extends continuously along a profile at 25°N , but gradually declines southward and concentrates at 101°E – 103°E beneath the Ailaoshan gold belt (Fig. S1). The S-wave velocity gradients (V_s/h) across the Moho show significant variations in the area. Bounded by the RRF, the V_s gradients in the Indochina block are generally higher than those to the northeast of the RRF. Along the RRF, especially to the north of $\sim 26^\circ\text{N}$, there is a low- V_s gradient zone. Similarly, a low- V_s gradient zone also exists along an NS-strike fault system corresponding to the

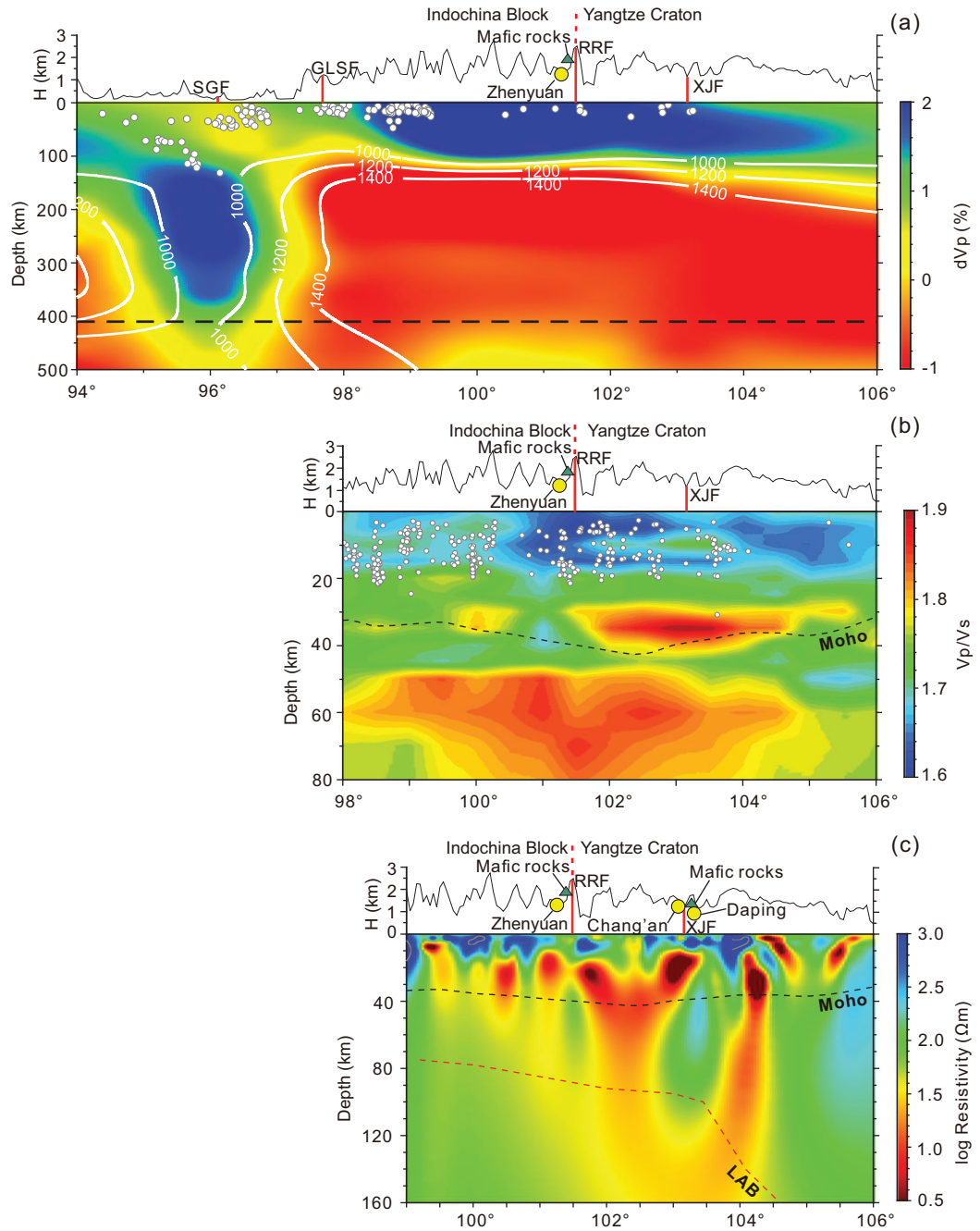


Figure 3. (a) The V_p structures along a profile at 24°N . The 1000°C , 1200°C and 1400°C adiabats of the upper mantle are estimated based on our determination of seismic velocity using the method from ref. [73]. Geological interpretation is given based on seismic velocity features and other geophysical data (see text). (b) Variation in V_p/V_s along a profile at 24°N . Two major domains of high V_p/V_s occur at the Moho (dashed line) and in the uppermost mantle. (c) MT 3D resistivity model projected on a profile near 24°N . Low-resistivity anomalies beneath the RRF and XJF trend steeply through the Moho and LAB into the asthenosphere. Abbreviation for faults same as Fig. 1b. Mafic dikes (triangles) and the Zhengyuan gold deposit (circles) are shown in (a–c).

Yuanyuan-Muliou fault (YMF) and XJF and ends at $\sim 24^\circ\text{N}$ (Fig. 2b).

The V_p/V_s model derived from joint inversion along a profile at 24°N clearly shows a large high V_p/V_s body in the uppermost mantle and two

distinct-scale high V_p/V_s anomalies near the Moho (33–40 km) (Fig. 3b). Such a spatially separated high V_p/V_s pattern across the Moho also appears in other profiles across the Ailaoshan gold belt (Fig. S2).

MT imaging results

A new 3D resistivity model shows that a resistor in the upper crust exists directly beneath the trace of the RRF and XJF, but that some locally spaced low-resistivity anomalies occur in the crust below the gold ore districts (Figs 3c, S3). In particular, there are at least three large low-resistivity anomalies near the Moho at 101–104°E (Fig. 3c). These extend upward into the middle-upper crust and connect to the low-resistivity anomalies below the gold ore deposits. Similar structures are also shown on other profiles from north to south (Fig. S3). Importantly, these low-resistivity anomalies at the Moho penetrate downward across the lithosphere-asthenosphere boundary (LAB) [53], converging into a significant conductor in the upper mantle (Fig. 3c) [33], which is broadly coincident with a high Vp/Vs body (Fig. 3b). Two relatively high-resistivity anomalies in the upper mantle spatially correspond to the Yangtze Craton and Indochina block, respectively (Fig. 3c), reflecting the trans-lithosphere conductors that occur along the boundary of convergent blocks.

Noble gas and halogen compositions of ore minerals

The He-Ar isotope ratios of disseminated gold ores are equivocal in terms of source as there is fluid-rock interaction during gold mineralization. However, the quartz vein ores, which reflect minimal fluid-rock reactions, are more likely to provide less equivocal indications of fluid source. We therefore analyzed the halogen compositions and noble gas isotope ratios of fluid inclusions hosted in both quartz and auriferous pyrite from samples of quartz vein gold ores hosted by diorite and dolomite at Daping (Supplementary Data, Tables S1–2).

Our results show that crushing quartz releases fluids with consistent molar Br/Cl (0.7×10^{-3} to 1.2×10^{-3}) and molar I/Cl ratios (12×10^{-6} to 34×10^{-6}), which are close to mantle values but contrast sharply with the atmosphere end-member (Fig. 4a). Crushing the pyrite samples released $3.7\text{--}12.0 \times 10^{-7}$ cm³ STP/g ⁴He and $0.7\text{--}1.6 \times 10^{-7}$ cm³ STP/g ⁴⁰Ar, and yielded a restricted range of ³He/⁴He (1.0–1.3 R/Ra) and ⁴⁰Ar/³⁶Ar (550 to 1680) ratios (Fig. 4b–d), close to but higher than previous results (0.1 to 1 R/Ra) [54,55]. The fluids trapped in both pyrite and quartz at Daping have consistent ⁴⁰Ar/³⁶Ar ratios (Supplementary Data, Tables S1–2), resembling those in the Jiaodong gold deposits with a demonstrated strong mantle contribution [56], but differing from those

of Macreas in New Zealand with a proposed predominantly crustal source (Fig. 4b, c) [57]. All samples at Daping have ³He/³⁶Ar ratios of $2\text{--}8 \times 10^{-3}$ (Fig. 4c), similar to mantle values, but higher than those of air-saturated water ($5\text{--}6 \times 10^{-8}$) [58].

Volatiles in lamprophyre dikes

We analyzed F and Cl contents of phlogopites and estimated pressure and temperature for lamprophyre dikes in the Ailaoshan gold belt (Supplementary Data, Table S3) to better understand relationships between lamprophyres and orogenic gold ores. Our results show that the phlogopites from lamprophyres not spatially associated with gold deposits in western Tethys (Alpine Orogen) have extremely low Cl/F ratios, which has been attributed to the lack of abundant volatiles in their source [59]. In contrast, the lamprophyre dikes spatially associated with both the Chang'an and Daping gold deposits have both demonstrably higher Cl/F ratios and distinctive distributions in terms of pressure-temperature (P-T) conditions compared to those in western Tethys (Fig. 5). The phlogopites in both gold deposits show a similar tendency, in which they first reach maximum Cl/F values at ~ 2.2 GPa and 1150°C, and then values rapidly decrease towards 1.2 GPa and 1050°C (Fig. 5).

DISCUSSION

Our study presents a number of geophysical models, including Vp, Vs, Vs/h and Vp/Vs, as well as resistivity at different scales around the Ailaoshan gold belt (Figs 2, 3). Similar models have been obtained in previous studies for Vp and Vs structure [60–62], Vp/Vs structure [63] and resistivity structure [33,64]. However, Vs/h across the Moho is obtained in the study area for the first time. The application of joint seismic inversion with three different data types helps to improve seismic images of the lithosphere. More densely spaced MT stations in this study also help to provide better electrical images of deep structure. More importantly, the conjunction of these diverse geophysical parameters enables us to reconstruct a more systematic and comprehensive picture of lithospheric structure in order to constrain the deep geodynamic processes that were capable of triggering gold mineralization. The lithospheric structure imaged by seismic and MT methods is the best approximation of the lithospheric structure at the time of mineralization. The mineralization slightly postdated the shearing along the Ailaoshan belt, block rotation of the Indochina block, and extensive magmatic intrusion

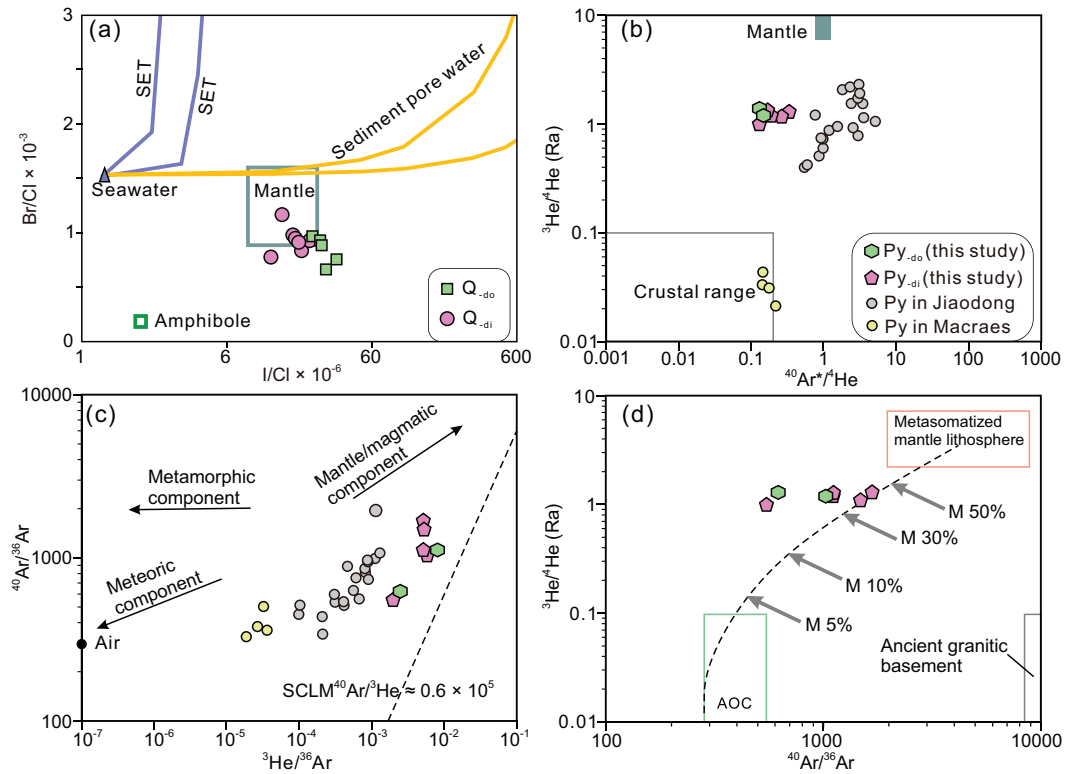


Figure 4. Halogen values and He-Ar isotopic compositions of fluid inclusions from gold-related quartz and pyrite of the Daping gold deposit. (a) I/Cl vs. Br/Cl plot for quartz. (b) ⁴⁰Ar*/⁴He vs. ³He/⁴He plot for pyrite. (c) ³He/³⁶Ar vs. ⁴⁰Ar/³⁶Ar plot for pyrite. (d) ⁴⁰Ar/³⁶Ar vs. ³He/⁴He plot for pyrite and binary mixing modeling for the fluid source. M equals mantle components. The mantle, crust, ancient granitic basement, air, amphibole and sedimentary pore water reference values are from ref. [58] and references therein. The reference values of sediments are from refs [112,113], of mantle halogen ratios from ref. [114], and of seawater from ref. [115] and references therein. The SCLM ⁴⁰Ar/³He reference values are from ref. [54]. Abbreviations: Py = pyrite, Py_{-di} = pyrite in diorite, Py_{-do} = pyrite in dolomite, Q_{-di} = ore quartz hosted in diorite, Q_{-do} = ore quartz hosted in dolomite, SCLM = subcontinental lithospheric mantle, SET = seawater trajectories.

in the western Yangtze block. Afterwards, the region basically entered a tectonic quiescent stage with crustal uplift and sporadic mafic dike intrusion along the Ailaoshan belt, which does not correspond to the heat flux in both space and intensity.

Lithospheric deformation and crust–mantle decoupling

The nature of lithosphere deformation and material flow in the southeastern Tibetan Plateau have been constrained using several geophysical imaging methodologies [28–32]. The crustal displacement fields determined by GPS measurements [26,27] indicate that the surface movement involved clockwise rotation around the East Himalayan syntaxis (Fig. 2a), suggesting nearly NS-trending crustal flow across the RRF [28]. However, the pattern of Vs gradients (Vs/h) across the Moho shows that this crustal flow may mainly occur to the north of ~26°N. Figure 2b displays two nearly NS-trending

low-Vs gradient zones along RRF and XJF, north of ~26°N, corresponding to two previously imaged low-velocity zones [65,66], interpreted to represent two crustal channel flows [67]. In contrast, south of 26°N, the Vs gradients across the Moho have distinct geographically restricted patterns. To the west of the RRF, a large high-Vs gradient domain spatially overlaps with the Indochina block, suggesting that the block is relatively rigid and lacks ductile crustal rheology and Moho reworking. To the east of the RRF, a low-Vs gradient zone, bounded by the Xiaojiang and Yuanyuan-Muliou faults, is truncated by the RRF at 24°N (Fig. 2b). Such an abrupt change suggests that crustal flow was likely blocked by the large-scale strike-slip RRF starting at ~26°N, where the Indochina block is interpreted to have been extruded along the RRF.

Many studies of seismic anisotropy in the southeastern Tibetan Plateau show that the polarization directions in the crust are dominantly N-S [67–70], consistent with geodetic estimates of crustal displacement (Fig. 2a) and the N-S-trending rock

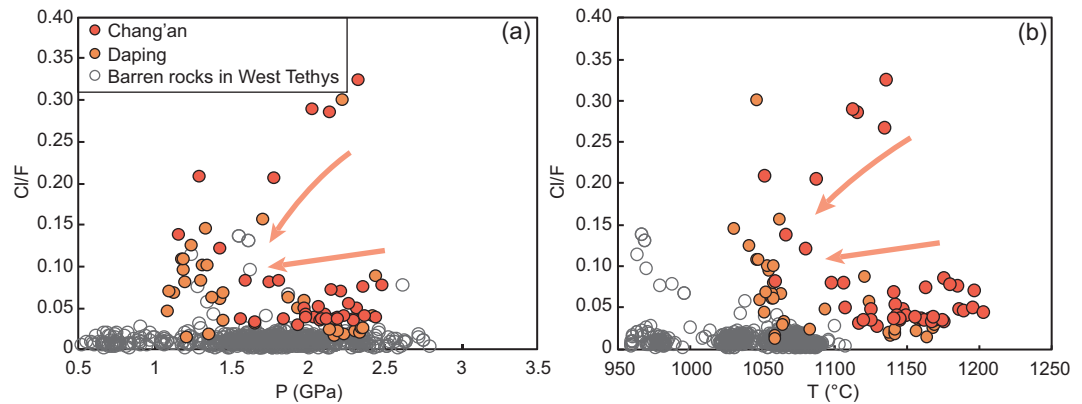


Figure 5. The Cl/F ratios of phlogopites, plus pressure and temperature calculated from phlogopites in lamprophyre dikes. (a) Cl/F vs. P. (b) Cl/F vs. T diagrams. The calculated temperature and pressure of phlogopite is based on refs [116–118]. The detailed calculation process is shown in the Supplementary Data. The Cl/F ratios of phlogopites in lamprophyre first increase and then decrease with a decrease in temperature and pressure.

fabrics interpreted to be caused by crustal compression and shearing. In contrast, the mantle anisotropy derived from analysis of teleseismic shear wave splitting has a pronounced transition in polarization direction from primarily N-S to mostly E-W around latitude 26°N (Fig. 2a) [28–30,62]. This transition reflects a fundamental change in the deformation regime within the southeastern margin of Tibet along the RRF. Recent seismic anisotropy studies have ascribed the E-W orientation of seismic anisotropy to deformation from the upper asthenosphere to the mantle lithosphere [32,62,71].

North of ~26°N, the anisotropy can be interpreted to represent coherent deformation between the crust and mantle lithosphere [28,30,72]. South of ~26°N, however, the SKS polarization directions do not correlate with known surface features and GPS measured data (Fig. 2a), implying that deformation between crust and mantle was mechanically decoupled [29]. It is noteworthy that this large-scale domain of decoupled deformation spatially overlaps with the extensive low-velocity body in the upper mantle (Fig. 2a). This decoupled deformation between crust and mantle constitutes a specialized architecture for the Ailaoshan gold belt.

Asthenosphere driving lithospheric crust–mantle decoupling

Our seismic V_p image demonstrates strong velocity heterogeneity in the upper mantle (Figs 2a, 3a). The profile at 24°N clearly depicts that the Indian lithosphere, as a high- V_p body, experienced high-angle subduction and reached the mantle transition zone (Fig. 3a). To the east of the subducted Indian slab, a large-magnitude mushroom-shaped low- V_p body extends laterally beneath the rigid Asian man-

tle lithosphere, with its stem rooted into the deep mantle (Fig. 3a). We interpret this effect as representing upwelling asthenosphere driven by eastward deep subduction of the Indian lithosphere. Our seismic images depict that the upper interface of the asthenosphere is at a depth of ~80 km (Fig. 3a), consistent with the LAB depth (80–100 km) beneath the Ailaoshan gold belt [53]. These data are consistent with extensive thinning of the overlying Asian lithosphere caused by upwelling asthenosphere.

Figure 3a denotes the adiabat of the upper mantle calculated using a velocity-temperature model [73], which defines a steep temperature gradient centered on the upwelling asthenosphere. We estimate that the mantle temperatures at ~80 km were up to 1000°C (Fig. 3a), consistent with those recorded by mantle xenoliths at Maguan (928–1110°C at 50–80 km [74]). This estimated temperature is also close to the estimated equilibrium temperatures (1007–1130°C) for the Quaternary basalts at Tengchong [75] and those (1000–1150°C) of Eocene lamprophyres along the RRF [76]. In addition, this mantle temperature approximates the solidus temperature of the H₂O-bearing mantle peridotite at similar pressures [77]. These data suggest that the upwelling asthenosphere provided enough heat for partial melting of the overlying Asian mantle lithosphere since the Eocene. At a deeper level of 82–120 km, where ocean-island basalts (OIBs) originate [78], the calculated mantle temperatures reach the lowest melting temperature (1200°C) of the mantle peridotite [77], but lower than the estimated equilibrium temperature (<1373°C) of the OIB magmas at Maguan [79]. This means that melt segregation from the limited partially melted upwelling asthenosphere could have led to the generation of OIB magmas.

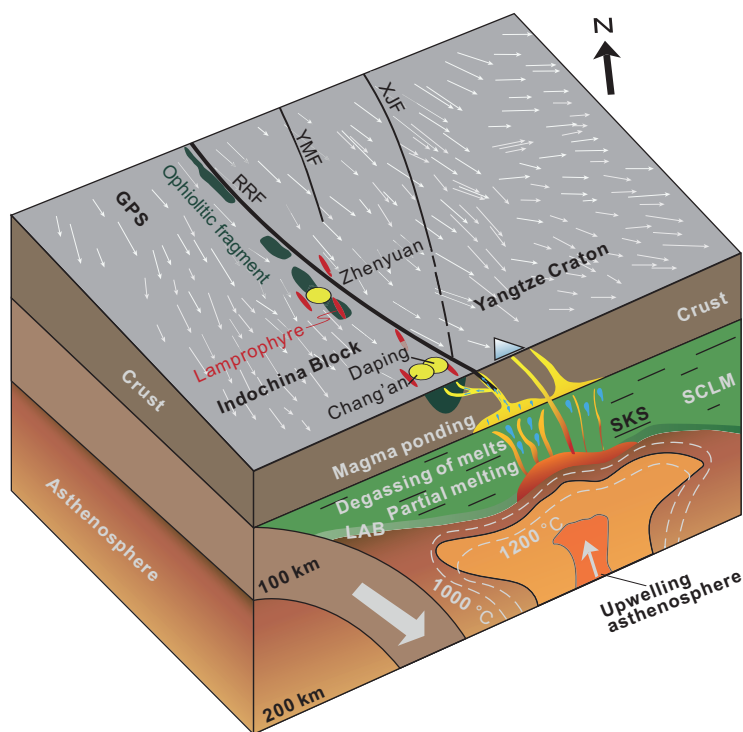


Figure 6. A cartoon illustrating a lithosphere architecture characterized by crust–mantle decoupling, constrained by geophysical and geological data, and its control over generation of orogenic gold deposits. The subduction of the Indian continent induced E–W-trending flow of mantle lithosphere driven by asthenosphere upwelling and NNW-trending crustal deformation, constituting an architecture characterized by crust–mantle decoupling. Controlled by this architecture, the RRF acted as a high-flux conduit, along which basic magma ponded and degassed, leading to formation of a series of OGDs at the fault intersections. Abbreviations: LAB = lithosphere–asthenosphere boundary; SCLM = subcontinental lithospheric mantle.

The above P–T estimates for the mantle lithosphere, combined with the temporal–spatial distribution of the Cenozoic magmatic rocks south of 26°N (Fig. 1b), further constrain a sub-lithosphere process beneath the Ailaoshan gold belt. This process is interpreted to include vertical upwelling of the asthenosphere that triggered mantle melting focused at 35 Ma, lateral flow that produced the Tengchong basalts at 14 Ma, and continued upwelling and melt segregation that generated E–W-trending sporadic OIB magmatic rocks since 13 Ma. We therefore suggest that vertical upwelling and lateral flow of the asthenosphere, driven by eastward deep subduction of the Indian continent during Cenozoic collision, caused E–W-directed deformation and extension of the overlying Asian mantle lithosphere (Fig. 6).

Heat-flow conduits and ponding of basic magma

The emplacement of the Eocene lamprophyre dikes along the RRF (Fig. 1b) suggests that this block

boundary fault likely provided a channel for heat flow from the upper mantle (Fig. 6), which is supported by low- V_s gradients across the reworked Moho by upwelling heat flow along the RRF (Fig. 2b). Seismic receiver functions analysis indicates that the converted phases at both Moho and LAB beneath the RRF show significant lateral discontinuities, suggesting a lithosphere-scale vertical discontinuity and mechanically weak zone [33]. The heat-flow data suggest that heat flow via this weak zone strongly modified the crustal thermal state beneath the RRF. For example, the lowermost crust at Dali, near the RRF, has an abnormally high geothermal temperature estimated as being up to 1000°C [80], thus triggering its melting to generate the Eocene gold-rich porphyries at Beiya [52]. The heat flow along the RRF also resulted in high-temperature granulite-facies metamorphism of the lower crust at 40–35 Ma [42].

Our MT model further constrains the heat-flow conduit across the Moho. It shows that the spherical conductors near the Moho extend downwards and converge into a large conductor in the upper mantle (Figs 3c, S3). This remarkable low-resistivity feature cannot easily be explained by the presence of relatively dry upper mantle, based on anhydrous mantle xenoliths [81], requiring the involvement of melt and/or water. The maximum melt fraction is up to 3% in the uppermost mantle, based on the analysis of mantle H^+ water and melt content [33]. This requires that the heat-flow conduits were rooted in the underlying mantle lithosphere containing a small amount of melt and traversed across the Moho along the Ailaoshan belt.

This interpretation is also consistent with our V_p/V_s model, which shows two spatially separated high V_p/V_s anomalies at 30–40 km and 60–80 km beneath the RRF (Fig. 3b). Theoretically, such high V_p/V_s ratios could be largely attributed to more mafic rocks and/or partial melts [82]. The high V_p/V_s body in the uppermost mantle (60–80 km) is rooted in the underlying asthenosphere as shown by the high-magnitude low-velocity anomaly (Fig. 3a, b), suggesting that the partially melted mantle lithosphere was heated by upwelling asthenosphere. High V_p/V_s anomalies at the base of the crustal base spatially coincide with the lower-crustal conductors that extend upward into gold ore districts (Fig. 3b, c, Fig. S4), consistent with a model in which hydrous basic to ultrabasic magmas ponded largely at the base of the crust, but partly intruded into the upper crust as lamprophyre dikes.

Integrated analysis of the V_p structure, V_p/V_s ratio and the MT model combined with geological observations indicates that ponding of mantle-derived basic magmas at the base of the crust was largely

concentrated at two locations along the RRF. The first is located east of the RRF, where the OGDs spatially occupy the edges of a Vp/Vs anomaly at a depth of 35 km (Fig. 2c). For example, the Zhenyuan gold district is located at an intersection between the RRF and YMF at $\sim 24^\circ\text{N}$ (Fig. 2c), where the crustal conductors coincide with a high Vp/Vs body in the lower crust (Fig. 3b, c), and Vs/h reflects strong velocity modification near the Moho (Fig. 2b). The Chang'an and Daping gold districts are located at an intersection of the RRF with the XJF at $\sim 23^\circ\text{N}$, where the high Vp/Vs mantle anomalies are spatially coincident with high mantle conductors beneath the gold districts (Fig. S4), and variation in Vs/h suggests a local thermal disturbance at the Moho (Fig. 2b). All these data lead us to conclude that the block boundary at the RRF provided channels for high heat flow from the partially melted mantle lithosphere, and that decoupling between crust and mantle deformation promoted ponding of basic magmas at the base of the crust with limited intrusion into the upper crust. The second ponding location is around Dali, where basic magmas ascended via heat-flow conduits and ponded at the base of the crust, leading to partial melting of the lower crust to generate hydrous magmas that were the parents of the porphyry-gold deposit at Beiya (Fig. 2c). We therefore argue that the lithospheric architecture that was characterized by crust–mantle decoupling and heat-flow conduits across the Moho had a profound impact on the formation of the Ailaoshan gold province.

Link between basic magmas and gold deposits

Phlogopites, as the largest and most abundant phenocrysts in lamprophyres, are able to dynamically re-equilibrate their composition in the melts [83], and thus can preserve a halogen record representative of the melt composition during crystallization [84]. The halogens, especially Cl and F, have been recently applied to trace and evaluate the role of magmatic volatiles, according to their sensitivity to volatile degassing [85] and their similar properties to incompatible elements [86]. The concentrations of halogens in a magma would gradually increase with its evolution and, accordingly, Cl/F ratios would increase due to the greater partition coefficient of Cl than F in volatile-rich melts such as those crystallizing lamprophyres. However, the exsolution of fluid by degassing would remove a large amount of Cl from the melt into the fluid, leading to a significant decrease in Cl/F ratios in the evolved magmas [87].

The Cl/F ratios of phlogopites from lamprophyres in the Ailaoshan gold belt continuously decrease, with P and T ranging from 2.4 GPa to 1.2 GPa

and 1150°C to 1050°C (Fig. 5). Cl/F ratios demonstrate a particularly rapid decrease at 1.2 GPa and 1050°C (Fig. 5), which corresponds to the depth of the crust–mantle boundary (35–40 km; Fig. 3) and the high geothermal temperature of up to 1000°C at the Moho [80]. This indicates that a large amount of Cl was extracted by degassing of the hydrous magmas at the interface of the crust–mantle transition. This degassing process is also recorded by some special textures of the lamprophyre dikes, such as gas cavities and abundant carbonate ocelli [34].

The noble gas and halogen contents and ratios of fluids trapped in ore minerals can constrain whether the fluid that exsolved from the basic magma has the capacity to generate gold ores, since the noble gases and halogens are normally stable during fluid transport [57,88] and therefore can effectively distinguish between different fluid reservoirs [89]. Previous He–Ar isotope analyses on fluid inclusions from gold-related pyrites yielded a range of $^3\text{He}/^4\text{He}$ of 0.1 to 1 R/Ra [54,90], suggesting a mantle contribution to the ore fluid [90]. Our new data show relatively high $^3\text{He}/^4\text{He}$ ratios (1.0 to 1.3 R/Ra) and $^3\text{He}/^{36}\text{Ar}$ ratios ($2\text{--}8 \times 10^{-3}$), confirming a significant contribution from mantle or degassing mantle melts to the ore fluid. In particular, the fluid inclusions from minerals in quartz vein orebodies have molar Br/Cl ratios of $0.7\text{--}1.2 \times 10^{-3}$ and I/Cl ratios of $12\text{--}34 \times 10^{-6}$, identical to those of mantle values (Fig. 4a), further demonstrating that ore fluids had the potential to be formed by degassing of hydrous basic magma at the base of the crust.

The conclusions obtained via new geochemical data are supported by Pb–S isotope data. The lamprophyre dikes have narrow ranges of $^{206}\text{Pb}/^{204}\text{Pb}$ (18.50–18.59), $^{207}\text{Pb}/^{204}\text{Pb}$ (15.60–15.65) and $^{208}\text{Pb}/^{204}\text{Pb}$ (38.75–38.84), which overlap with those of gold-related sulfides in the Ailaoshan gold belt (Supplementary Data) [91,92]. The gold-rich rims of ore pyrites uniformly display a limited range of $\delta^{34}\text{S}$ values around 0‰ [6,93,94], similar to those expected for a mantle source for the lamprophyre dikes that are spatially related to the gold deposits.

The lamprophyre dikes themselves have too low a volume to directly exsolve ore fluid to form the gold deposits but provide a link to related but larger-volume subcrustal magma-related devolatilization processes that do have this capacity. Thus, the spatially and temporally related gold deposits and lamprophyres do not have a direct genetic relationship but are indirectly connected to a similar mantle lithosphere source and belong to the different consequences of the same mantle process. The platinum group element (PGE) analyses carried out in a previous study have shown that the basic magma has

witnessed sulfide saturation and separation [6,95], which would increase the fertility of the fluid source.

Crustal conduits for ore fluid migration

Our MT imaging reveals vertical or oblique high-strength conductors in the middle-upper crust (Figs 3c, S4). For example, a high-strength conductor that is inclined to the NE extends obliquely downward to 40 km beneath the Zhenyuan ore district (Fig. 3c). Similarly, two high-strength conductors beneath the Chang'an and Daping ore districts intersect near the Moho (Fig. S3). These conductors cannot be explained by the widely exposed high-grade metamorphic rocks in the Ailaoshan belt, which typically display low conductivity [33]. A possible interpretation is that the ophiolitic fragments or oceanic relics, which survived underneath the Ailaoshan belt [96] and were strongly replaced by heat fluid flows, migrated along the faults. This is similar to the MT structures, called Fingers of God, from below the supergiant Olympic Dam iron-oxide copper-gold deposit, which are interpreted to represent fluid pathways that extended from the mantle lithosphere across the Moho into the upper crust [97].

The results from this study, in combination with reassessment of previously published He-Ar isotopic data [54,90], provide clues related to the involvement of the ophiolitic fragments or oceanic relics in the formation or modification of auriferous ore fluids in the Ailaoshan belt. The varied $^3\text{He}/^4\text{He}$ ratios of 0.03–1.34 Ra and $^{40}\text{Ar}/^{36}\text{Ar}$ ratios of 310–4020 of the auriferous fluids indicate that they contain a component of altered oceanic crust (AOC) (Fig. 4d), in addition to a component from metasomatized mantle lithosphere, the lamprophyre source. Binary mixing modeling of $^3\text{He}/^4\text{He}$ and $^{40}\text{Ar}/^{36}\text{Ar}$ ratios suggests that the AOC components account for 30% (Fig. 4d). It is most likely that the AOC components were derived from serpentinized ultramafic rocks, altered oceanic relics, in the ophiolitic melanges that were under-thrust northeastward along the steeply dipping ALF [33]. These serpentinized ultramafic rock blocks are interpreted to represent crustal fluid conduits, in which lithological heterogeneities were utilized by advecting ore fluids. The water/rock interaction during fluid migration in the middle-upper crust could have increased the fluid fertility.

Lithospheric control over orogenic gold deposits and its implications

Our results show that the lithospheric architecture was essentially characterized by mechanical decou-

pling between crust and mantle, formed as a result of asthenosphere upwelling and lateral flow. This architecture promoted the partial melting of metasomatized mantle lithosphere and provided a favorable space for ponding and degassing of mantle-derived melts and a well-linked structural architecture for transport of melts and fluids, thus controlling the evolution of the Ailaoshan orogenic gold system.

Such a lithospheric structure, characterized by crust–mantle decoupling, is also interpreted for world-class giant gold provinces worldwide. The Jiaodong gold province was formed during the transition of subduction direction of the Pacific plate from NW to NNW at ca. 120 Ma [4,9]. The strike-slip movement along the Tanlu fault, a trans-lithospheric fault in the Jiaodong Peninsula, was NNE-trending, nearly perpendicular to the SKS fast direction in the mantle [98], thus showing the feature of crust–mantle decoupling (Fig. 6). Such a lithospheric structure promotes the degassing of the hydrous basic magmas at the base of the crust or during ascent, as suggested by previous studies based on the close spatial-temporal association between the mafic dikes and gold deposits in the Jiaodong gold belt [12,99]. Similarly, in the Xiaoqinling Orogen, central China, the crust with E-W-trending movement overlaps the underlying upper mantle with an N-S-trending SKS fast direction [100]. Moreover, in South China, the NE-trending orogenic belt overlies a nearly N-S-trending mantle SKS fast direction [101]. The Juneau gold belt, Alaska, along the Pacific eastern subduction zone, is also a potential analog of the Ailaoshan and Jiaodong gold provinces. This gold belt formed at ~55 Ma, when a change from orthogonal to oblique subduction caused a shift from thrusting to strike-slip motion on the NNW-trending ore-controlling Sumdum and Fanshaw faults [102]. All these examples indicate that the critical architecture characterized by crust–mantle decoupling is typically formed during a transition period between tectonic regimes, driven by change in drift direction of the subducting plate and the orientation of the crust in orogenic settings. The obvious discrepancy between the subduction direction and orientation of crustal deformation reflects a lithospheric architecture characterized by crust–mantle decoupling, in which the orogenic gold deposits discussed above formed.

The reason why crust–mantle decoupling is beneficial for gold mineralization is that it has the capacity to connect the following processes that occur at different depths in the crust–mantle system. They include: (i) a deep thermal engine represented by upwelling asthenosphere, which triggered partial melting of metasomatized mantle lithosphere to

generate basic-ultrabasic magma; (ii) crust–mantle decoupling, which provided a dilatational space for ponding and degassing of the basic magma at the base of the crust; and (iii) crustal-scale strike-slip faults that serve as heat-flow conduits for magma intrusion and fluid migration. We suggest that crust–mantle decoupling provides an optimal configuration related to a transition in tectonic regime, coincident with the presence of trans-lithosphere faults, and mafic dike emplacement, that is critical to the formation of specific orogenic gold deposits. Such lithosphere architecture is normally developed at craton or thick lithosphere margins, which provide high-quality exploration targets for a variety of ore deposit types [103]. From another perspective, the metallogenic model proposed here implies that despite the fact that asthenosphere upwelling can occur in different tectonic regimes [103,104], it is only capable of triggering gold mineralization with the additional key parameters of mantle lithosphere compositions and geometries, trans-crustal and trans-lithosphere structures, and suitable trap rocks and structures. This metallogenic model provides a new lithospheric control and petrological and geochemical constraints on the subcrustal model for the formation of OGDs.

CONCLUSIONS

The multidisciplinary research carried out in this study has reconstructed the architecture of the lithosphere on the southeastern margin of Tibet and deciphered its control over the formation of OGDs along the Ailaoshan gold belt. The area is characterized by a lithosphere that was shaped by the decoupled deformation of crust and mantle that was, in turn, driven by deep Indian continental subduction. This architecture facilitated the development of heat-flow conduits and exerted structural control over the generation of OGDs. The formation of OGDs was initiated by mantle partial melting, basic magma ponding and fluid release at the base of the crust, as well as fluid migration in the middle-upper crust with similar geophysical signatures to that of the supergiant Olympic Dam iron-oxide copper-gold deposit. Similar lithosphere architecture is recognized in some giant gold provinces, implying that analogous geodynamic processes controlled their formation.

METHODS

To image the lithosphere structure for the Ailaoshan gold belt, we jointly used seismic and MT imaging methods. For seismic imaging, we adopted a multi-scale strategy to first image mantle structure

for southwest China using the teleseismic double-difference tomography method [105]. We then produced a V_p/V_s model of the lithosphere and the velocity gradients across the Moho by joint inversion of seismic body wave arrival times, surface wave dispersion data and receiver functions [106]. The details of different inversions and results are given in the Supplementary Data.

For MT imaging, based on the previous 3D electrical resistivity model of the lithosphere in the area [33], we added two horizontal (at 24°N and 25°N) and longitudinal profiles (at 100°E and 101°E), with the total MT stations increasing from 173 to 309 (Supplementary Data). The electromagnetic inversion system ModEM [107,108] was used to invert the full impedance tensor with a homogeneous 100 Ωm half-space starting model. The final total RMS (root mean square) misfit value reached 2.20 after 160 iterations (Supplementary Data), and a new more refined resistivity model with a wider area than the previous model [33] was obtained (Figs 3, S3). The details of the inversion and the model are presented in the Supplementary Data file.

The $\sim 70\text{-mg}$ -sized aliquots of high-purity separates of gold-related quartz that were irradiated in the McClellan Research Reactor Center at UC Davis were analyzed by crushing steps *under a vacuo condition*. A MAP215-50 noble gas mass spectrometer was used to expand the purified noble gases for Ar isotope analysis, with the data reduction based on ref. [109]. The 1 sd uncertainties for Br/Cl and I/Cl are $\sim 3\%$ and $\sim 5\%$, respectively [110]. Helium and Ar isotopes of ore pyrites were measured at the Institute of Geology and Geophysics, Chinese Academy of Sciences, Beijing, using the Helix SFT mass spectrometer. The operating procedures and sample measurements data can be found in refs [111,112].

Electron probe microanalysis (EPMA), for major-element analysis of phlogopite, was carried out at the Geological Analysis Unit (GAU), Macquarie University, using a Cameca SX-100 electron microprobe with five wavelength-dispersive spectrometers. Minerals were analyzed using a 15 kV accelerating voltage, with a beam current of 20 nA and diameter of 1–2 μm . Counting times were 10 s for peak and 5 s for background measurements on each side of the peak. Natural minerals and synthetic oxides were used as standards for correction [119]. The temperature and pressure calculation for phlogopite are given in the Supplementary Data.

SUPPLEMENTARY DATA

Supplementary data are available at [NSR](https://doi.org/10.1093/nsr/nvac257) online.

ACKNOWLEDGEMENTS

We are grateful to four anonymous reviewers for providing constructive comments during review.

FUNDING

This work was supported by the National Natural Science Foundation of China (U1839205 to H.Z., 42121002 to R.W., 42074081 to N.Y., 42125203 to Q.F. and 42102107 to Y.L.), the National Key Research and Development Program of China (2022YFF0800903 to Z.H.), the Strategic Priority Research Program of the Chinese Academy of Sciences (XDB 41000000 to H.Z.), the Fundamental Research Funds for the Central Universities (WK2080000 to H.Z.) and the Project of the Ministry of Science and Technology (BP0719021).

AUTHOR CONTRIBUTIONS

ZQ.H. designed and initiated the research, interpreted the data and wrote most of the manuscript. QF.W. interpreted ore geochemistry data and wrote some of the manuscript. HJ.Z. supervised and conducted seismic tomography analysis and wrote some of the manuscript. N.Y. supervised and conducted MT analysis and wrote some of the manuscript. B.X. interpreted lamprophyre data and wrote some of the manuscript. D.I.G. provided some new concepts and an intensive English edit. All authors contributed to the discussion and interpretation of results.

Conflict of interest statement. None declared.

REFERENCES

- Groves DI, Goldfarb RJ and Gebre-Mariam M *et al.* Orogenic gold deposits: a proposed classification in the context of their crustal distribution and relationship to other gold deposit types. *Ore Geol Rev* 1998; **13**: 7–27.
- Goldfarb RJ, Baker T and Dubé B *et al.* Distribution, character, and genesis of gold deposits in metamorphic terranes. In: Hedenquist JW, Thompson JFH and Goldfarb RJ (eds.). *Economic Geology One Hundredth Anniversary Volume*. Littleton, Colorado: Society of Economic Geologists Inc, 2005; 407–50.
- Kerrick R. Nature's gold factory. *Science* 1999; **284**: 2101–2.
- Goldfarb RJ, Hart C and Davis G *et al.* East Asian gold: deciphering the anomaly of Phanerozoic gold in Precambrian cratons. *Econ Geol* 2007; **102**: 341–5.
- Tomkins AG. On the source of orogenic gold. *Geology* 2013; **41**: 1255–6.
- Wang Q, Groves DI and Deng J *et al.* Evolution of the Miocene Ailaoshan orogenic gold deposits, southeastern Tibet, during a complex tectonic history of lithosphere-crust interaction. *Miner Depos* 2020; **55**: 1085–104.
- Deng J, Wang Q and Santosh M *et al.* Remobilization of metasomatized mantle lithosphere: a new model for the Jiaodong gold province, eastern China. *Miner Depos* 2020; **55**: 257–74.
- Deng J, Qiu KF and Wang QF *et al.* In-situ dating of hydrothermal monazite and implications on the geodynamic controls of ore formation in the Jiaodong gold province, eastern China. *Econ Geol* 2020; **115**: 671–85.
- Deng J, Yang LQ and Groves DI *et al.* An integrated mineral system model for the gold deposits of the giant Jiaodong province, eastern China. *Earth-Sci Rev* 2020; **208**: 103274.
- Hou Z and Cook NJ. Metallogensis of the Tibetan collisional orogen: a review and introduction to the special issue. *Ore Geol Rev* 2009; **36**: 2–24.
- Zhu R, Zhang H and Zhu G *et al.* Craton destruction and related resources. *Int J Earth Sci (Geol Rundsch)* 2017; **106**: 2233–57.
- Wang Q, Yang L and Zhao H *et al.* Towards a universal model for orogenic gold systems: a perspective based on Chinese examples with geodynamic, temporal, and deposit-scale structural and geochemical diversity. *Earth-Sci Rev* 2022; **224**: 103861.
- Deng J, Liu X and Wang Q *et al.* Isotopic characterization and petrogenetic modeling of Early Cretaceous mafic dike—lithospheric extension in the North China craton, eastern Asia. *Geol Soc Am Bull* 2017; **129**: 1379–407.
- Kazansky VI and Yanovsky VM. The correlation of Mesozoic gold ore districts at the Sino-Korean and Aldan-Stanovoi shields. *Geol Ore Depos* 2006; **48**: 43–60.
- Deng J, Wang C and Bagas L *et al.* Cretaceous–Cenozoic tectonic history of the Jiaojia Fault and gold mineralization in the Jiaodong Peninsula, China: constraints from zircon U–Pb, illite K–Ar, and apatite fission track thermochronometry. *Miner Depos* 2015; **50**: 987–1006.
- Chen Y, Fyee WS and Zang W *et al.* Thoughts on the Jiaodong gold province of China: towards a tectonic model. *Acta Geol Sin-Engl* 1999; **73**: 1–7.
- Groves DI, Santosh M and Deng J *et al.* A holistic model for the origin of orogenic gold deposits and its implications for exploration. *Miner Depos* 2020; **55**: 275–92.
- Hou Z, Zaw K and Pan G *et al.* Sanjiang Tethyan metallogenesis in S.W. China: tectonic setting, metallogenic epochs and deposit types. *Ore Geol Rev* 2007; **31**: 48–87.
- Sun X, Zhang Y and Xiong D *et al.* Crust and mantle contributions to gold-forming process at the Daping deposit, Ailaoshan gold belt, Yunnan, China. *Ore Geol Rev* 2009; **36**: 235–49.
- Deng J, Wang Q and Li G *et al.* Cenozoic tectono-magmatic and metallogenic processes in the Sanjiang region, southwestern China. *Earth-Sci Rev* 2014; **138**: 268–99.
- Yang L, Wang Q and Groves DI *et al.* Mineral assemblages, fluid inclusions, pyrite trace elements, and S–O isotopes of gold ores from the Cenozoic Daping deposit, SW China: implications for the genesis of complex orogenic lode gold systems. *Econ Geol* 2021; **110**: 487–511.
- Goldfarb RJ and Groves DI. Orogenic gold: common or evolving fluid and metal sources through time. *Lithos* 2015; **233**: 2–26.
- Wyman DA, Cassidy KF and Hollings P. Orogenic gold and the mineral systems approach: resolving fact, fiction and fantasy. *Ore Geol Rev* 2016; **78**: 322–35.
- Zhao H, Wang Q and Groves DI *et al.* A rare Phanerozoic amphibolite-hosted gold deposit at Danba, Yangtze Craton, China: significance to fluid and metal sources for orogenic gold systems. *Miner Depos* 2019; **54**: 133–52.

25. Zhao H, Wang Q and Kendrick MA *et al.* Metasomatized mantle lithosphere and altered ocean crust as a fluid source for orogenic gold deposits. *Geochim Cosmochim Acta* 2022; **334**: 316–37.
26. Zhang PZ, Shen Z and Wang M *et al.* Continuous deformation of the Tibetan Plateau from global positioning system data. *Geology* 2004; **32**: 809–12.
27. Gan W, Zhang P and Shen Z-K *et al.* Present-day crustal motion within the Tibetan Plateau inferred from GPS measurements. *J Geophys Res: Solid Earth* 2007; **112**: B08416.
28. Lev E, Long M and Vanderhilst R. Seismic anisotropy in Eastern Tibet from shear wave splitting reveals changes in lithospheric deformation. *Earth Planet Sci Lett* 2006; **251**: 293–304.
29. Sol S, Meltzer A and Bürgmann R *et al.* Geodynamics of the southeastern Tibetan Plateau from seismic anisotropy and geodesy. *Geology* 2007; **35**: 563.
30. Chang L, Ding Z and Wang C. Upper mantle anisotropy beneath the southern segment of North-South tectonic belt, China (in Chinese). *Chin J Geophys* 2015; **58**: 4052–67.
31. Liang C, Liu Z and Hua Q *et al.* The 3D seismic Azimuthal anisotropies and velocities in the eastern Tibetan plateau extracted by an Azimuth-dependent dispersion curve inversion method. *Tectonics* 2020; **39**: e2019TC005747.
32. Huang Z and Chevrot S. Mantle dynamics in the SE Tibetan Plateau revealed by teleseismic shear-wave splitting analysis. *Phys Earth Planet Inter* 2021; **313**: 106687.
33. Yu N, Unsworth M and Wang X *et al.* New insights into crustal and mantle flow beneath the Red River fault zone and adjacent areas on the southern Margin of the Tibetan plateau revealed by a 3-D magnetotelluric study. *J Geophys Res Solid Earth* 2020; **125**: e2020JB019396.
34. Huang XL, Niu Y and Xu YG *et al.* Mineralogical and geochemical constraints on the petrogenesis of post-collisional potassic and ultrapotassic rocks from western Yunnan, SW China. *J Petrol* 2010; **51**: 1617–54.
35. Lu YJ, Kerrich R and Mccuaig TC *et al.* Geochemical, Sr-Nd-Pb, and Zircon Hf-O isotopic compositions of eocene-oligocene shoshonitic and potassic adakite-like felsic intrusions in western Yunnan, SW China: petrogenesis and tectonic implications. *J Petrol* 2013; **54**: 1309–48.
36. Yin A and Harrison TM. Geologic evolution of the Himalayan-Tibetan orogen. *Annu Rev Earth Planet Sci* 2000; **28**: 211–80.
37. Wang J, Qi L and Yin A *et al.* Emplacement age and PGE geochemistry of lamprophyres in the Laowangzhai gold deposit, Yunnan, SW China. *Sci China Ser D-Earth Sci* 2001; **44**: 146–54.
38. Zhou M, Ma Y and Yan D *et al.* The Yanbian Terrane (Southern Sichuan Province, SW China): a Neoproterozoic arc assemblage in the western margin of the Yangtze Block. *Precambrian Res* 2006; **144**: 19–38.
39. Liu J, Song Z and Cao S *et al.* The dynamic setting and processes of tectonic and magmatic evolution of the oblique collision zone between Indian and Eurasian plates: exemplified by the tectonic evolution of the Three River region, eastern Tibet (in Chinese with English abstract). *Acta Petrol Sin* 2006; **22**: 775–86.
40. Searle MP, Yeh M-W and Lin T-H *et al.* Structural constraints on the timing of left-lateral shear along the Red River shear zone in the Ailao Shan and Diancang Shan Ranges, Yunnan, SW China. *Geosphere* 2010; **6**: 316–38.
41. Liu F, Wang F and Liu P *et al.* Multiple partial melting events in the Ailao Shan–Red River and Gaoligong Shan complex belts, SE Tibetan Plateau: zircon U–Pb dating of granitic leucosomes within migmatites. *J Asian Earth Sci* 2015; **110**: 151–69.
42. Liu F, Wang F and Liu P *et al.* Multiple metamorphic events revealed by zircons from the Diancang Shan–Ailao Shan metamorphic complex, southeastern Tibetan Plateau. *Gondwana Res* 2013; **24**: 429–50.
43. Socquet A and Pubellier M. Cenozoic deformation in western Yunnan (China–Myanmar border). *J Asian Earth Sci* 2005; **24**: 495–515.
44. Guo Z, Hertogen J and Liu J *et al.* Potassic magmatism in Western Sichuan and Yunnan provinces, SE Tibet, China: petrological and geochemical constraints on petrogenesis. *J Petrol* 2005; **46**: 33–78.
45. Hou Z, Xu B and Zheng Y *et al.* Mantle flow: the deep mechanism of large-scale growth in Tibetan Plateau. *Chin Sci Bull* 2021; **66**: 2671–90.
46. Sun X, Xiong D and Shi G *et al.* ⁴⁰Ar/³⁹Ar dating of gold deposit hosted in the Daping ductile shear zone in the Ailaoshan gold belt, Yunnan Province (in Chinese). *Acta Geol Sin* 2007; **81**: 88–92.
47. Gao L, Wang Q and Deng J *et al.* Relationship between orogenic gold mineralization and crustal shearing along Ailaoshan-Red river belt, southeastern Tibetan plateau: new constraint from paleomagnetism. *Geochem Geophys Geosyst* 2018; **19**: 2225–42.
48. Yang L, Wang Q and Groves DI *et al.* Multiple orogenic gold mineralization events in a collisional orogen: insights from an extruded terrane along the southeastern margin of the Tibetan Plateau. *J Struct Geol* 2021; **147**: 104333.
49. Ying H, Wang D and Liu H. Geology and formation time of nickel mineralization in Jinchang nickel-gold deposit, Mojiang, Yunnan (in Chinese with English abstract). *Miner Depos* 2005; **1**: 44–51.
50. Wang Q, Deng J and Weng W *et al.* Cenozoic orogenic gold system in Tibet (in Chinese). *Acta Petrol Sin* 2020; **36**: 1315–53.
51. Deng J, Wang Q and Li G *et al.* Geology and genesis of the giant Beiya porphyry–skarn gold deposit, northwestern Yangtze Block, China. *Ore Geol Rev* 2015; **70**: 457–85.
52. Hou Z, Zhou Y and Wang R *et al.* Recycling of metal-fertilized lower continental crust: origin of non-arc Au-rich porphyry deposits at cratonic edges. *Geology* 2017; **45**: 563–6.
53. Hu J, Yang H and Li G *et al.* Seismic upper mantle discontinuities beneath southeast Tibet and geodynamic implications. *Gondwana Res* 2015; **28**: 1032–47.
54. Burnard PG, Hu R and Turner G *et al.* Mantle, crustal and atmospheric noble gases in Ailaoshan gold deposits, Yunnan Province, China. *Geochim Cosmochim Acta* 1999; **63**: 1595–604.
55. Hu RZ, Burnard PG and Bi XW *et al.* Helium and argon isotope geochemistry of alkaline intrusion-associated gold and copper deposits along the Red River–Jinshajiang fault belt, SW China. *Chem Geol* 2004; **203**: 305–17.
56. Tan J, Wei J and He H *et al.* Noble gases in pyrites from the Guocheng–Liaoshang gold belt in the Jiaodong province: evidence for a mantle source of gold. *Chem Geol* 2018; **480**: 105–15.
57. Goodwin NR, Burgess R and Craw D *et al.* Noble gases fingerprint a metasedimentary fluid source in the Macraes orogenic gold deposit, New Zealand. *Miner Depos* 2017; **52**: 197–209.
58. Kendrick MA and Burnard P. Noble gases and halogens in fluid inclusions: a journey through the Earth’s crust. In: Burnard P (ed.). *The Noble Gases as Geochemical Tracers*. Berlin, Heidelberg: Springer, 2013, 319–69.
59. Muller D and Groves D. Potassic igneous rocks and associated gold-copper mineralization. In: Müller D and Groves DI (eds.). *Mineral Resource Reviews*. Berlin, Heidelberg: Springer, 2019, 1–398.
60. Wang CY, Lou H and Silver PG *et al.* Crustal structure variation along 30 N in the eastern Tibetan Plateau and its tectonic implications. *Earth Planet Sci Lett* 2010; **289**: 367–76.
61. Wei W, Xu J and Zhao D *et al.* East Asia mantle tomography: new insight into plate subduction and intraplate volcanism. *J Asian Earth Sci* 2012; **60**: 88–103.

62. Kong F, Wu J and Liu L *et al.* Azimuthal anisotropy and mantle flow underneath the southeastern Tibetan Plateau and northern Indochina Peninsula revealed by shear wave splitting analyses. *Tectonophysics* 2018; **747–8**: 68–78.
63. Zhang Y, Wang B and Xu T *et al.* Three-dimensional crustal Vp and Vs structures beneath the southern segment of the Tan-Lu fault revealed by active source and earthquake data. *Geophys J Inter* 2020; **223**: 2148–65.
64. Ye T, Chen X and Liu Z *et al.* A magnetotelluric study of 3D electrical resistivity structure underneath the southern segment of the Red River fault zone, South China. *J Asian Earth Sci* 2022; **225**: 105056.
65. Gao Y, Shi Y and Wang Q. Seismic anisotropy in the southeastern margin of the Tibetan Plateau and its deep tectonic significances (in Chinese). *Chin J Geophys* 2020; **63**: 802–16.
66. Bao X, Sun X and Xu M *et al.* Two crustal low-velocity channels beneath SE Tibet revealed by joint inversion of Rayleigh wave dispersion and receiver functions. *Earth Planet Sci Lett* 2015; **415**: 16–24.
67. Liu C, Yao H and Yang H-Y *et al.* Direct inversion for three-dimensional shear wave speed azimuthal anisotropy based on surface wave ray tracing: methodology and application to Yunnan, southwest China. *J Geophys Res Solid Earth* 2019; **124**: 11394–413.
68. Yao H, van der Hilst RD and Montagner J-P. Heterogeneity and anisotropy of the lithosphere of SE Tibet from surface wave array tomography. *J Geophys Res* 2010; **115**: B12307.
69. Sun Y, Niu F and Liu H *et al.* Crustal structure and deformation of the SE Tibetan plateau revealed by receiver function data. *Earth Planet Sci Lett* 2012; **349–50**: 186–97.
70. Huang Z, Wang L and Xu M *et al.* P Wave anisotropic tomography of the SE Tibetan Plateau: evidence for the crustal and upper-mantle deformations. *J Geophys Res Solid Earth* 2018; **123**: 8957–78.
71. Zhang Z, Yao H and Yang Y. Shear wave velocity structure of the crust and upper mantle in Southeastern Tibet and its geodynamic implications. *Sci China Earth Sci* 2020; **63**: 1278–93.
72. Shi Y, Gao Y and Su Y *et al.* Shear-wave splitting beneath Yunnan area of Southwest China. *Earthq Sci* 2012; **25**: 25–34.
73. An M and Shi Y. Lithospheric thickness of the Chinese continent. *Phys Earth Planet Inter* 2006; **159**: 257–66.
74. Xia P and Xu Y. Mantle-derived xenoliths in Maguan Cenozoic potassic basalt, southeast Yunnan and its bearing on lithospheric composition and dynamics (in Chinese with English abstract). *Geochimica (Beijing)* 2006; **35**: 1–5.
75. Yang S, Humayun M and Salters VJ. Elemental constraints on the amount of recycled crust in the generation of mid-oceanic ridge basalts (MORBs). *Sci Adv* 2020; **6**: eaba2923.
76. Xu B, Hou Z-Q and Griffin WL *et al.* Cenozoic lithospheric architecture and metallogenesis in Southeastern Tibet. *Earth-Sci Rev* 2021; **214**: 103472.
77. Collins WJ, Murphy JB and Johnson TE *et al.* Critical role of water in the formation of continental crust. *Nat Geosci* 2020; **13**: 331–8.
78. Huang Y, Chubakov V and Mantovani F *et al.* A reference Earth model for the heat-producing elements and associated geoneutrino flux. *Geochem Geophys Geosyst* 2013; **14**: 2003–29.
79. Wang Z. Tectonic evolution of the Hengshan–Wutai–Fuping complexes and its implication for the Trans-North China Orogen. *Precambrian Res* 2009; **170**: 73–87.
80. Zhou Z and Xiang C. Distribution of the lithospheric geotemperature in Yunnan (in Chinese with English abstract). *Seismol Geol* 1997; **19**: 227–34.
81. Constable S. SE03: a new model of olivine electrical conductivity. *Geophys J In* 2006; **166**: 435–7.
82. Christensen NI. Poisson's ratio and crustal seismology. *J Geophys Res* 1996; **101**: 3139–56.
83. Foley SF, Venturelli G and Green DH *et al.* The ultrapotassic rocks: characteristics, classification, and constraints for petrogenetic models. *Earth-Sci Rev* 1987; **24**: 81–134.
84. Rock NM, Groves DI and Perring CS *et al.* Gold, lamprophyres, and porphyries: what does their association mean. *Econ Geol Monogr* 1989; **6**: 609–25.
85. Maria AH and Luhr JF. Lamprophyres, basanites, and basalts of the Western Mexican volcanic belt: volatile contents and a Vein–Wallrock melting relationship. *J Petrol* 2008; **49**: 2123–56.
86. Balcone-Boissard H, Villemant B and Boudon G *et al.* Non-volatile vs volatile behaviours of halogens during the AD 79 plinian eruption of Mt. Vesuvius, Italy. *Earth Planet Sci Lett* 2008; **269**: 66–79.
87. Aiuppa A, Baker DR and Webster JD. Halogens in volcanic systems. *Chem Geol* 2009; **263**: 1–18.
88. Fairmaid AM, Kendrick MA and Phillips D *et al.* The origin and evolution of mineralizing fluids in a sediment-hosted orogenic-gold deposit, Ballarat East, southeastern Australia. *Econ Geol* 2011; **106**: 653–66.
89. Kendrick MA, Honda M and Walshe J *et al.* Fluid sources and the role of abiogenic-CH₄ in Archean gold mineralization: constraints from noble gases and halogens. *Precambrian Res* 2011; **189**: 313–27.
90. Hu RZ, Burnard P and Bi XW *et al.* Mantle-derived gaseous components in ore-forming fluids of the Xiangshan uranium deposit, Jiangxi province, China: evidence from He, Ar and C isotopes. *Chem Geol* 2009; **266**: 86–95.
91. Li WC, Wang JH and He ZH *et al.* Formation of Au-polymetallic ore deposits in alkaline porphyries at Beiya, Yunnan, Southwest China. *Ore Geol Rev* 2016; **73**: 241–52.
92. Xu XW, Zhang BL and Qin KZ *et al.* Origin of lamprophyres by the mixing of basic and alkaline melts in magma chamber in Beiya area, western Yunnan, China. *Lithos* 2007; **99**: 339–62.
93. Li H, Wang Q and Deng J *et al.* Source and evolution of ore fluids in the Zhenyuan orogenic gold deposit, SE Tibet: constraints from the S-C-O isotopes. *Ore Geol Rev* 2020; **121**: 103534.
94. Yang L, Wang Q and Large RR *et al.* Fluid source and metal precipitation mechanism of sediment-hosted Chang'an orogenic gold deposit, SW China: constraints from sulfide texture, trace element, S, Pb, and He-Ar isotopes and calcite C-O isotopes. *Am Mineral* 2021; **106**: 410–29.
95. Gan T and Huang Z. Platinum-group element and Re-Os geochemistry of lamprophyres in the Zhenyuan gold deposit, Yunnan Province, China: implications for petrogenesis and mantle evolution. *Lithos* 2017; **282–3**: 228–39.
96. Lin TH, Chung SL and Chiu HY *et al.* Zircon U–Pb and Hf isotope constraints from the Ailao Shan–Red River shear zone on the tectonic and crustal evolution of southwestern China. *Chem Geol* 2012; **291**: 23–37.
97. Heinson G, Didana Y and Soeffky P *et al.* The crustal geophysical signature of a world-class magmatic mineral system. *Sci Rep* 2018; **8**: 10608.
98. Li H, Song X and Lü Q *et al.* Seismic imaging of lithosphere structure and upper mantle deformation beneath East-Central China and their tectonic implications. *J Geophys Res Solid Earth* 2018; **123**: 2856–70.
99. Wang Z, Cheng H and Zong K *et al.* Metasomatized lithospheric mantle for Mesozoic giant gold deposits in the North China Craton. *Geology* 2020; **48**: 169–73.
100. Zhang G, Meng Q and Lai S. Tectonics and structure of Qinling orogenic belt. *Sci China Series B* 1995; **11**: 1379–94.

101. Hou J, Xu T and Lv Q *et al.* The deep background of the large-scale Mesozoic Cu-Au-W metallogenesis in the northeastern South China: constraints from Yingshan-Changshan wide-angle seismic reflection/refraction data. *Sci China Earth Sci* 2022; **65**: 2202–18.
102. Goldfarb RJ, Leach DL and Pickthorn WJ *et al.* Origin of lode-gold deposits of the Juneau gold belt, southeastern Alaska. *Geology* 1988; **16**: 2202–18.
103. Groves DI and Santosh M. Craton and thick lithosphere margins: the sites of giant mineral deposits and mineral provinces. *Gondwana Res* 2021; **100**: 195–222.
104. Green DH and Falloon TJ. Mantle-derived magmas: intraplate, hot-spots and mid-ocean ridges. *Sci Bull* 2015; **60**: 1873–900.
105. Pesicek JD, Zhang H and Thurber CH. Multiscale seismic tomography and earthquake relocation incorporating differential time data: application to the maule subduction zone, Chile. *Bull Seismol Soc Am* 2014; **104**: 1037–44.
106. Han S, Zhang H and Gao L *et al.* Joint inversion of body wave arrival times, surface wave dispersion data and receiver functions: method and application to south China. *J Geophys Res Solid Earth* 2022; **127**: e2022JB024083.
107. Egbert GD and Kelbert A. Computational recipes for electromagnetic inverse problems. *Geophys J Int* 2012; **189**: 251–67.
108. Kelbert A, Meqbel N and Egbert GD *et al.* ModEM: a modular system for inversion of electromagnetic geophysical data. *Comput Geosci* 2014; **66**: 40–53.
109. Kendrick MA. High precision Cl, Br and I determinations in mineral standards using the noble gas method. *Chem Geol* 2012; **292–3**: 116–26.
110. Kendrick MA, Arculus R and Burnard P *et al.* Quantifying brine assimilation by submarine magmas: examples from the Galápagos Spreading Centre and Lau Basin. *Geochim Cosmochim Acta* 2013; **123**: 150–65.
111. He H, Zhu R and Saxton J. Noble gas isotopes in corundum and peridotite xenoliths from the eastern North China Craton: implication for comprehensive refertilization of lithospheric mantle. *Phys Earth Planet Inter* 2011; **189**: 185–91.
112. Matsuda J, Matsumoto T and Sumino H *et al.* The $^3\text{He}/^4\text{He}$ ratio of the new internal He Standard of Japan (HESJ). *Geochem J* 2002; **36**: 191–5.
113. Staudacher T and Allègre CJ. Recycling of oceanic crust and sediments: the noble gas subduction barrier. *Earth Planet Sci Lett* 1988; **89**: 173–83.
114. Holland G and Ballentine CJ. Seawater subduction controls the heavy noble gas composition of the mantle. *Nature* 2006; **441**: 186–91.
115. Chavrit D, Burgess R and Sumino H *et al.* The contribution of hydrothermally altered ocean crust to the mantle halogen and noble gas cycles. *Geochim Cosmochim Acta* 2016; **183**: 106–24.
116. Guo J and Green TH. Experimental study of barium partitioning between phlogopite and silicate liquid at upper-mantle pressure and temperature. *Lithos* 1990; **24**: 83–95.
117. Righter K and Carmichael ISE. Phase equilibria of phlogopite lamprophyres from western Mexico: biotite-liquid equilibria and P-T estimates for biotite-bearing igneous rocks. *Contrib Mineral Petrol* 1996; **123**: 1–21.
118. Xu B, Hou ZQ and Griffin WL *et al.* Apatite halogens and Sr–O and zircon Hf–O isotopes: recycled volatiles in Jurassic porphyry ore systems in southern Tibet. *Chem Geol* 2022; **605**: 120924.
119. Xu B, Hou ZQ and Griffin WL *et al.* Recycled volatiles determine fertility of porphyry deposits in collisional settings. *Am Mineral* 2021; **106**: 656–61.